ACS APPLIED MATERIALS & INTERFACES
Research Article
www.acsami.org

Fundamental Resolution Limits during Electron-Induced Direct-Write Synthesis

Georg Arnold,[†] Rajendra Timilsina,[‡] Jason Fowlkes,[§] Angelina Orthacker,[∥] Gerald Kothleitner,[†,∥] Philip D. Rack,[‡,§] and Harald Plank*[,†,∥]

[†]Institute for Electron Microscopy and Nanoanalsis, Graz University of Technology, Steyrergasse 17, 8010 Graz, Austria
[‡]Department of Materials Science and Engineering, University of Tennessee, Knoxville, Tennessee 37996, United States
[§]Center for Nanophase Materials Sciences, Oak Ridge National Laboratory, Oak Ridge, Tennessee 37831, United States
[∥]Graz Centre for Electron Microscopy, Steyrergasse 17 8010 Graz, Austria

Supporting Information

ABSTRACT: In this study, we focus on the resolution limits for quasi 2-D single lines synthesized via focused electron-beam-induced direct-write deposition at 5 and 30 keV in a scanning electron microscope. To understand the relevant proximal broadening effects, the substrates were thicker than the beam penetration depth and we used the MeCpPt(IV)Me_3 precursor under standard gas injection system conditions. It is shown by experiment and simulation how backscatter electron yields increase during the initial growth stages which broaden the single lines consistent with the backscatter range of the deposited material. By this it is shown that the beam diameter together with the evolving backscatter radius of the deposit material determines the achievable line widths even for ultrathin deposit heights in the sub-5-nm regime.

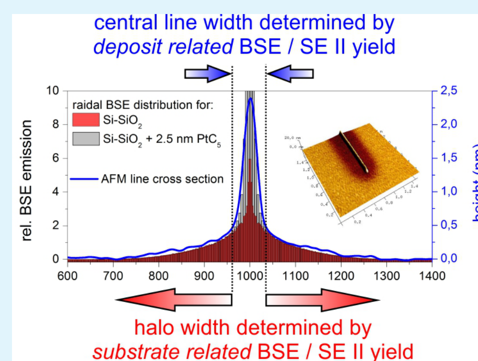

KEYWORDS: *focused electron-beam-induced deposition, platinum, nanofabrication, Monte Carlo simulations, atomic force microscopy, transmission electron microscopy*

INTRODUCTION

Direct-write synthesis of functional structures with nanometer resolution is currently a grand challenge that has the potential to revolutionize science and technology provided it can be done fast and with minimal pre- or post-growth treatment. Focused electron-beam-induced deposition (FEBID) is one technique that basically allows such direct-write nanofabrication and has attracted increasing attention during the last decade as an increasing number of applications have been demonstrated. FEBID works with a gaseous precursor which is locally decomposed by the electron beam into non-volatile functional components and volatile fragments which are pumped away from the chamber.[1−5] More specifically, the precursor molecules adsorb and diffuse on the surface for a typical residence time after which they can desorb from the surface. The balance between precursor molecules on the surface and available electrons, denoted as precursor working regime, can influence growth rates, deposit shapes and the deposit chemistry.[1−3,6−8] Depending on the precursor, final deposits allow a diverse range of application such as nanolithography,[9,10] lithography-mask repair,[11−13] nano optics,[14,15] atomic-layer-deposition seeding,[16] magnetic storage, sensing and logic applications,[17−21] nanoscale stress-strain sensors,[22,23] or gas sensors.[24] Because of the ongoing downscaling trends, FEBID's high-resolution capabilities are of particular importance. As previously shown, transmission electron microscopes (TEM) can be used to fabricate single "dots" down to the sub-nanometer range which demonstrates the ultimate resolution limited by the precursor chemistry.[25−33] Also free standing 1D pillars with a width of 5 nm[34] or single lines with a half pitch of 3 nm fabricated on thick Si substrates have been demonstrated.[35] However, these very impressive experiments mostly use special conditions, such as high energy electrons (TEM), together with sub-10-nm substrates or very low precursor coverage. From a more technological point of view, it is essential to understand what ultimately limits the achievable lateral resolution for a more ubiquitous scanning electron microscope (SEM) together with thick or bulk substrates and classically used precursor coverage which provides acceptable growth rates and by that high throughput. Several experimental and simulation studies have been performed which significantly improved the understanding of the processes including total cross sections for the precursor molecules, energy resolved electron emission, precursor regimes, proximity effects and others.[1,3,36−44] Very recently, van Dorp et al. concluded from experiments and simulations that secondary electrons (SE) generated in the substrate play a major role during very early growth stages.[31] Subsequently, the SE emission increases

Received: February 7, 2014
Accepted: April 24, 2014
Published: April 24, 2014

© 2014 American Chemical Society

because it gets more dominated by the deposit itself which finally approaches a constant value even if the deposit continues to grow. This regime change from substrate-dominated toward deposit-dominated electron emission is found to take place for very low deposit volumes in early growth stages.[31] On the basis of the experimental setup of using TEM and ultrathin carbon substrates between 1.4 and 4.3 nm the important contribution of backscatter electrons (BSE) is strongly reduced due to the limited interaction volume and the high electron energies used.[1−3,45] For bulk substrates in combination with typically used primary electron energies between 1 and 30 keV in, for example, SEMs, the BSE contribution and its entailed generation of type II SEs, is expected to be much higher and can play an essential role.

In this study, we focus on the achievable lateral resolutions during FEBID and its underlying mechanism using beam energies of 5 and 30 keV together with Si bulk substrates. $MeCpPt(IV)Me_3$ precursor have been used to deposit single lines as a function of beam current, pixel dwell time, and point pitch while always using single-pass patterns. The experiments have been complemented by Monte Carlo simulations and reveal BSE emission caused by the deposit itself similar to what has been demonstrated for SE emission by van Dorp et al.[31]

EXPERIMENTS AND RESULTS

Parameter Constraints. Since the highest lateral resolution was the aim of this study, only single-pass lines were done to minimize the influence of lateral drift and beam placement of subsequent electron passes. The second constraint was the highest allowable pixel pulse duration, further denoted as *pixel dwell time* (DT), of 4 ms for our microscope. The third demand concerned the line heights: (1) the lower limit was chosen to be around 2 nm since typical Pt grains are found in this size range (see Supporting Information Figure S1)[1−3,23,46] and (2) the upper limit was chosen to be about 50 nm in order to allow a reliable analysis via atomic force microscopy (AFM) with respect to the tip convolution (see Supporting Information Figure S2). Pre-experiments revealed a reasonable range for the point pitch (PoP) describing the pixel-to-pixel distance between neighbouring patterning points. To prevent discontinuous line heights an upper PoP limit of 20 nm has been chosen[43,49] while the lower PoP limit was set to 5 nm to prevent deposit lift off from the surface for smaller PoPs.[47−49] In order to stay between the specified line heights, beam currents ranging from 25 to 98 pA and 150 to 630 pA have been used for 5 and 30 keV, respectively. The two primary electron energies have been chosen to demonstrate the influence of substrate related backscatter electrons (BSE), and its related secondary electrons type II (SE-II), on final achievable lateral resolutions.

Representative AFM height images are shown in Figure 1 with the overlaid AFM phase information to reveal material contrast. For 30 keV (a), comparably sharp single lines are found which is also observed in the lower panel by the relevant AFM cross section. In contrast, for 5 keV lines (b), the overlaid phase signal clearly shows halo formation (dark areas) in the range of about ±300 nm around the FEBID single line. As can be seen by height cross sections in the lower panel of Figure 1b, the halo gradually increases towards the central line. The maximum heights for the halos vary depending on the line height but are always found clearly below 10 % of the absolute line height (a more detailed discussion will be provided later).

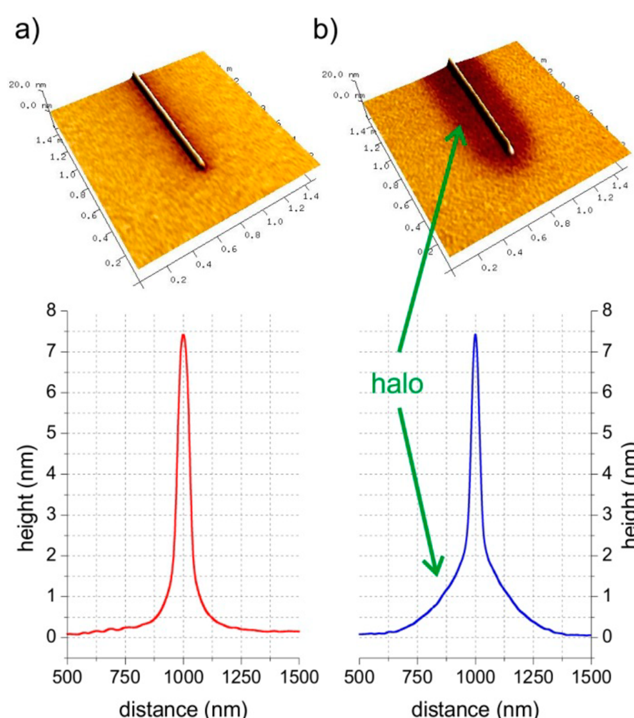

Figure 1. Direct comparison of AFM height images for 7.5 nm high Pt-C single lines fabricated with 30 (a) and 5 keV (b). The colors represent the AFM phase signal and reflect different composition. Associated line cross sections are given below and reveal the morphological halo for 5 keV lines (right cross section) which are not found for high primary energies (left cross section). Also the phase signal does not suggest a different composition in the proximity of the line for 30 keV (a).

Simulations. Figure 2 shows simulations of the radial BSE distribution for the used $Si-SiO_2$ (3 nm) substrate calculated via CASINO[50] further normalized to unit areas (see methodology). Note, for simplicity substrate (**S**) related BSE and the resultant SE-II emission are further denoted as BSE-S and SE-II-S. The upper panel in Figure 2a shows the radial BSE-S for 30 keV electrons and a beam diameter of 4 nm (FWHM)[51] for a lateral range of ±4000 nm on a logarithmic Y scale to visualize the long range contributions as a consequence of the spatially large interaction volume due to the high primary energy (see also Supporting Information Figure S3). The lower panel in Figure 2a gives a closer look within a range of ±400 nm, relevant for further discussions revealing negligible BSE-S contribution outside a radius of about ±50 nm. In contrast, Figure 2b shows the radial BSE-S distribution per unit area for 5 keV electrons with the same beam diameter (4 nm) revealing enhanced BSE-S contribution up to about ±300 nm. This is a consequence of the smaller interaction volume for lower primary energies (see also Supporting Information Figure S3), which also entails a higher BSE yield.[1,45] The simulated BSE-S radius of ±300 nm (Figure 2b) is in good agreement with the experimentally observed halo radius (AFM cross section in Figure 1b) which allows the assignment to substrate related backscattered electrons (BSE-S). The absence of a halo formation for 30 keV in Figure 1a together with the BSE simulations in Figure 2a suggests that the 30 keV experiments are virtually free from BSE-S contributions. To simplify the discussion we start with the 30 keV beam energy to discuss line

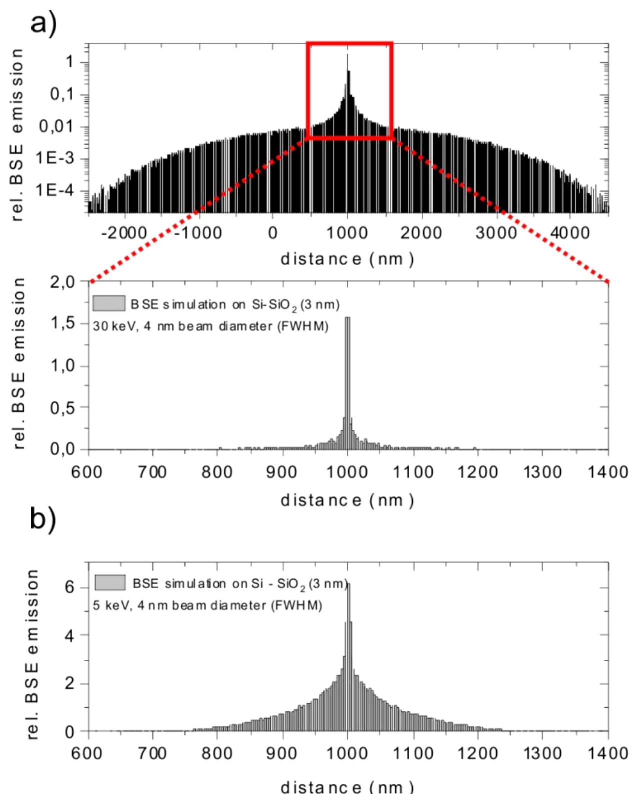

Figure 2. Simulated radial BSE distributions on Si-SiO_2 (3 nm) for 30 keV (a) assuming 4 nm beam diameter (FWHM) on logarithmic Y scale to reveal the far-reaching BSE radius. The lower panel in (a) shows the central area of ±400 nm and reveal a quickly decaying BSE contribution within ±50 nm around the beam center. The BSE contribution of 5 keV electrons is shown in (b) revealing the large proximal BSE contribution (compare directly to the upper panel for the 30 keV situation).

broadening effects followed by the 5 keV case including substrate related influences.

30 keV Single Lines. As a first step, the lateral scaling of the FWHM widths is summarized as a function of dwell times DT in Figure 3a for 630 (top) and 150 pA (bottom). The different symbols represent different point pitches PoP, indicated by the legend. As can be seen for both currents there is an initial increase followed by a more constant FWHM for higher DTs. A comparison with the line heights (right panels in Figure 3) reveals that the widths start to saturate for line heights around 2−4 nm for both currents. Figure 4 shows cross sectional profiles (solid lines, right axis) together with radial BSE distributions for the Si-SiO_2 (3 nm) substrate (dark red bars) and for differently thick PtC_5 layers (gray bars) according to the observed line heights. Airey disk estimations of the 30 keV electron beam diameters are 4 and 7 nm (FWHM) for 150 and 630 pA, respectively, which are both much smaller than the simulated BSE radii. As can be seen for low currents (a and b), the experimental line cross section and the simulated BSE emission profiles (gray bars) show very good agreement in terms of the lateral expansion and decay behaviour. A detailed look at Figure 4a shows a comparison of the cross sectional profile for a 1 nm high single line (blue solid line) together with the simulated radial BSE distribution (gray bars) as well as the BSE-S emission of the substrate (dark red bars). As can be seen, even a 1 nm thick PtC_5 layer results in a broadened emission profile which corresponds well with the experimental

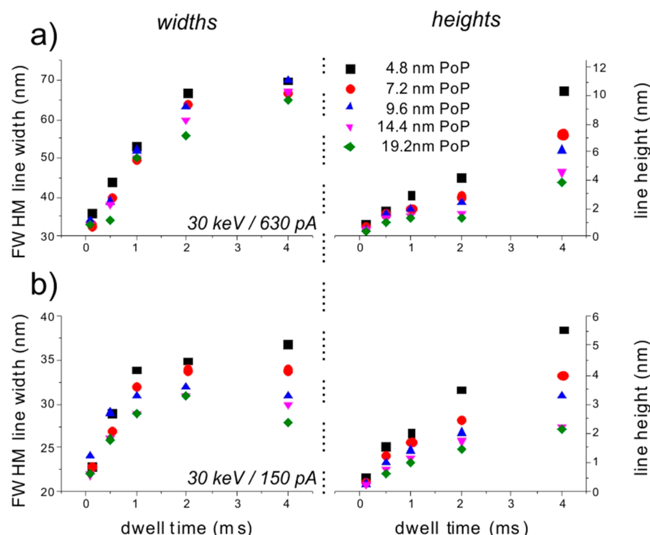

Figure 3. FWHM line widths (left column) and line heights (right columns) for 30 keV single lines fabricated at 630 (a) and 150 pA (b) as a function of the beam dwell time for different PoPs (see legend).

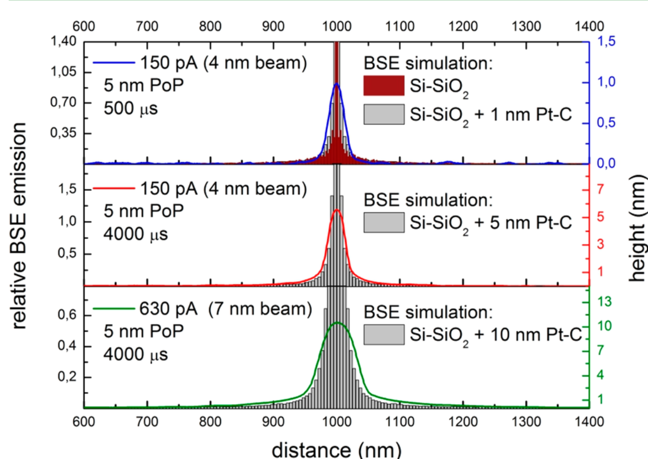

Figure 4. BSE simulation (bars, left axes) vs AFM line cross section (solid lines, right axes) for 30 keV primary electron energies assuming 4 (a and b) and 7 nm (c) beam diameter (FWHM) according to 150 and 630 pA, respectively. The simulations assume Pt−C layers of different thickness (see legends) with a Pt content of 15 at. % on Si substrates with 3 nm SiO_2 top layers.

observation (compare gray bars with the blue line) while the pure BSE-S distribution is found to be more narrow and of slightly different shape (dark red bars). This implies that immediately after the initial deposition events the total BSE distribution is already influenced by the deposit leading to line broadening. Increasing PtC_5 layer thicknesses from 1 (a) to 5 nm (b) leads to further broadening of the BSE distribution (gray bars) which again agrees well with the experiments (red solid line in Figure 4b). Thus, we attribute the slightly increasing line width in the sub-5-nm regime to PtC_5 related BSE and SE-II contributions which are further denoted as BSE-Pt and SE−II-Pt. For increasing beam currents the single line width increases even further (green solid line in Figure 4c), which, however, is again found to be in good agreement with the total radial BSE distribution considering base width and distribution shape (gray bars in Figure 4c). To correlate the line widths with the respective beam diameters for different beam currents we compared two single lines (both around 4 nm

high) synthesized at low and high beam currents (see Supporting Information Figure S4a). The lateral expansion was renormalized by the relevant electron-beam diameters according to $(2 \cdot r/\mathrm{FWHM_B})^1$ to compensate for different beam diameters. Both curves are found to be practically identical (see Supporting Information Figure S4b), which is in agreement with the constant BSE−Pt radius for both beam currents. Hence, from these experiments and simulations it can be deduced that for a given beam radius the finally achievable line width is determined by the radial BSE-Pt and the associated SE−II-Pt distribution of the growing Pt−C deposit which is a function of the progressive line height.

5 keV Single Lines. Similar experiments have been performed with a primary energy of 5 keV. The solid line in Figure 5a shows a cross section of a 2.5 nm high single line compared to simulated BSE distributions for a 2.5 nm PtC_5 layer on top of the $Si\text{-}SiO_2$ substrate (gray bars). The first thing to notice is the broader BSE distribution for the substrate (BSE-S) which has its maximum slightly above 300 nm in good agreement with simulations shown in Figure 2b (see also Supporting Information Figure S5). Nevertheless, the line width and its decay behaviour including the proximity halo are found in excellent agreement with the total BSE emission (gray bars). To separate substrate- and deposit-related BSE contributions the BSE-S emission of the $Si\text{-}SiO_2$ (3 nm) substrate is shown by the transparent dark red bars in Figure 5a. As demonstrated the halo attributed to BSE emission around the central line is identical which further supports the hypothesis of a substrate-related BSE-S contribution for the 5 keV halo formation. In contrast, the central BSE emission is clearly different in shape and intensity which suggests that the line itself again is more governed by BSE-Pt contributions from the growing deposit. While the lateral width and decay behaviour is found to be very similar to the AFM cross sectional profiles the central BSE intensity, howver, suggests higher vertical growth than observed via experiments. To investigate this effect in more detail, Monte Carlo simulations have been conducted to provide more insight in the local precursor molecule density. As a first step, the simulations have been adapted to mimic the vertical growth rate dependency observed for the dwell time DT. Very good agreement has been found for initial gas coverage of 7% (see Supporting Information Figure S6) using a typical residence time of 100 μs and a surface diffusion coefficient of 1×10^{-8} cm s^{-2} for the beam/processing parameters used (details can be found in the Methods).[1,3,38,39,52] Using this parameter set the local precursor depletion is estimated which is then compared to AFM cross sectional profiles (blue line) and BSE simulations (gray bars) in Figure 5b for a small range of ±25 nm around the line center. As shown by the red dashed curve for a pixel dwell time of 4000 μs, the surface coverage drops to essentially zero at the center of the beam. To estimate how the precursor coverage varies with dwell time, simulations were also performed with DTs of 1000 (dashed blue) and 100 μs (dashed green), which also shows a very strong depletion of the precursor molecule coverage at the beam center. Comparing the different precursor coverage indicates that the coverage progresses to a more depleted state at longer dwell times as expected. Thus, the picture emerges that the central beam area is depleted of precursor and therefore, even though the local electron flux is high, it is limited by the available precursor. Beyond this area, the electron flux is lower, however, the precursor population is much higher and thus experiences more efficient growth. This can explain the discrepancy between the higher simulated BSE contribution at the beam center (gray bars in Figure 5b) compared to the finally achieved FEBID lines observed via AFM (blue solid line in Figure 5b).

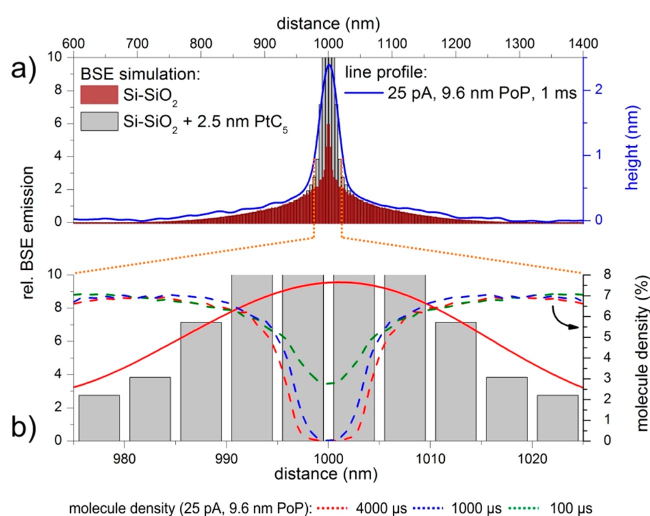

Figure 5. (a) BSE simulation (bars, left axes) for 5 keV primary electron energies assuming 4 nm beam diameter (FWHM) according to 25 pA beam current on $Si\text{-}SiO_2$ (gray bars) and for ~2.5 nm PtC_5 on $Si\text{-}SiO_2$ (gray bars) together with the associated AFM line cross section (blue solid lines, right axes). The lower panel gives the simulated precursor coverage (dashed lines) for a smaller area around the beam center for 4000, 1000, and 100 μs dwell time (see legend at the bottom) together with the BSE distribution (gray bars) and AFM line cross section (red solid line).

Finally, Figure 6 shows the summary of FWHM line widths (left) and line heights (right) where width-saturation is found for shorter dwell times (> 0.5 ms) compared to 30 keV (Figure 3). Considering the lower energy, the smaller interaction volume and by that the increased surface yield of electron species together with the higher dissociation cross section, it becomes evident that the higher efficiency for lower primary energies[41,42] leads to a faster volume growth rates (and by that

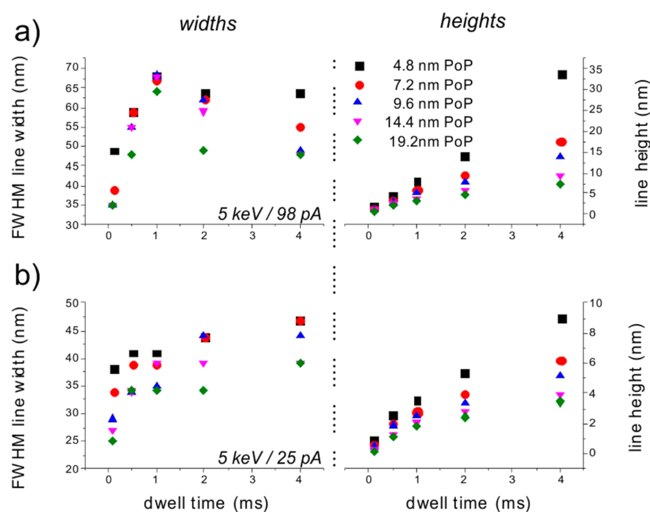

Figure 6. FWHM base widths (left column) and line heights (right columns) for 5 keV single lines fabricated at 98 (a) and 25 pA (b) as a function of the beam dwell time for different PoPs (see legend).

to faster saturation). Comparing the line width saturation points with the associated line heights (right panels in Figure 6b) reveals a transition between 2 and 5 nm line height very similar to 30 keV results (see Figure 3). This suggests the formation of the first granular Pt layer as the determining factor as will be discussed below.

DISCUSSION

From both experimental series we have observed that the line widths initially increase followed by more stable FWHM widths (30 and 5 keV in Figure 3 and Figure 6, respectively) for corresponding line heights between 2 -5 nm. This thickness range correlates with the initial formation of Pt grains, typically found in the range of 2−3 nm (see also Supporting Information Figure S1). Accordingly, BSE simulations confirmed that the presence of thin Pt−C layers lead to a broadening of the total, lateral BSE distribution which allows assignment of the line broadening to BSE-Pt species generated within the thin Pt−C deposits. Considering, the relatively low cross section for high energy BSEs,[41,42] it is likely that the associated SE-II cascades are predominantly responsible for the dissociation processes which, however, are strongly connected to the spatial BSE contribution. By that it is suggested that the line width is initially dominated by substrate related electron species followed by a transition towards more deposit related effects. This is in agreement with recent findings by Van Dorp et-al[31] who used TEM together with ultrathin carbon substrates (1.4−4.3 nm) to investigate the initial stages of the FEBID growth. They also reported this substrate-to-deposit related transition, however, mainly based on primary electron related SE-I species as the BSE yield (and by that SE-II contributions) for the high energies used is very low. The generally broader line widths found for our experiments compared to van Dorps findings (sub-10 nm FWHM line widths) can be explained by higher beam diameter in SEMs together with bulk substrates and the BSE/SE-II related broadening and might represent a more practical result instead of the ultimate possible resolution from a more chemical point of view.[31] However, considering again the BSE simulations in Figures 4 (30 keV) and 5 (5 keV), it is obvious that although lateral expansion and decay behaviour fits very well to experimental observations the central BSE yield would imply higher growth rates at the line centre than observed by the experiments. To explain this contradiction the local surface coverage has to be taken into account as shown in Figure 5b (dashed lines) for different dwell times DT. As can be seen, even for the shortest beam pulses of 100 μs the central coverage is slightly decreased which leads to lower central growth rates. This can explain the local mismatch between the central BSE emission and final growth while lateral expansion and decay behaviour matches the total BSE distribution very well (red line and gray bars in Figure 5a). Summarily it can therefore be stated that initial growth is dominated by primary electrons, secondary electrons type I (SE-I) and to a lower extent BSE-S and SE−II-S,[38−40,44] and subsequently the electron regime changes towards a deposit-driven BSE-Pt/SE−II-Pt rate within the first 5 nm (line heights) which finally determines the achievable line width.

As the described findings are a correlation between the deposit composition and fundamental electron behaviour in solids the above mentioned explanations are assumed to hold for other precursor materials and substrates although the extent of broadening will be different and a function of the beam parameters and the relative BSE yields of the deposit and substrate. It should also be noted, that this BSE-Pt growth concept can also explain the typically observed dimensions of 1D nanopillars between 50 and 70 nm for MeCpPt(IV)Me_3 precursor on bulk substrates[1−3,7,8,38] which are in the same range as the BSE-Pt diameter in contrast to the electron beams which often are an order of magnitude smaller.

Finally, the proximity halo (see Figure 1b) and its scaling behaviour for low primary energies is addressed. Figure 7 shows

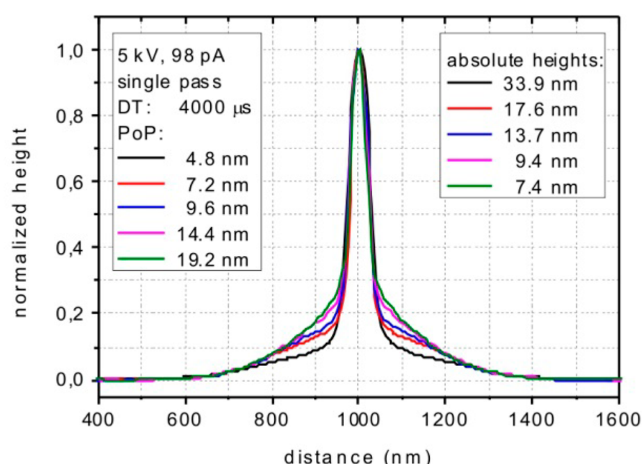

Figure 7. Normalized comparison of AFM line cross sections for 5 keV, 98 pA, and 4000 μs dwell time for different point pitches (left legend) revealing a decrease in the halo for increasing line heights (right legend).

a set of normalized cross sections of single lines fabricated at 5 keV/98 pA at 4 ms DT with varying PoPs (see left inset). Comparing the line profiles with the associated heights, specified in the right inset, one can note two details: (1) the relative height of the substrate related halo decreases with increasing line heights as a result of the decreasing number of electrons, which can enter the substrate and generate BSE-S related SE-II and much more importantly (2) the lines themselves show very similar widths, which is further indication that once the first granular Pt layer has evolved (2−5 nm) the widely constant BSE-Pt radius (for the thin deposits considered) determines the achievable line width for a given energy and chemical composition of the deposit. Although heights of the proximity halos are in the lower nm range nm range even for tall single lines (see Supporting Information Figure S7) the functionality has to be kept in mind as the halo is coupled to the the functional line. Hence, whenever targeting the highest functional lateral resolution, high primary energies should be used to prevent the formation of proximal halo deposition caused by substrate related BSE-S and SE-II-S contributions.

METHODS

Deposition experiments were performed with a FEI NOVA 200 (FEI, the Netherlands) dual beam system equipped with a FEI gas injection systems (GIS) for Pt−C deposition using a MeCpPt(IV)Me_3 precursor. 15 × 15 mm^2 Si samples with 3 nm SiO_2 were used and prepared in a laminar flow box for experiments. After immediate transfer of the samples to the dual beam microscope chamber a background pressure of at least 8 × 10^{-6} mbar has been established before any experiment was conducted. The precursor was pre-heated to 45 °C for at least 30 min. Beam focusing and optimization have been performed on different areas than the final experiments to prevent any cross contamination. Prior to any deposition, the GIS

nozzle has been opened for at least 3 min to provide a stable thermodynamic equilibrium between adsorption and desorption. The chamber pressure typically increased to a stable value of 2×10^{-5} mbar during deposition. Electron column sample distance was 5 mm for all experiments. Stage movements to defined areas have been performed with a blanked e-beam followed by deposition and an additional stage movement away from the actual deposition area. All patterns used 4096 × 4096 pixel bitmaps which contain vertically arranged spots. Deposition was then performed using 9.75 μm horizontal field of view, which allows a pixel resolution of ~2.4 nm. After successful deposition the structures have been characterized via atomic force microscopy (AFM) performed with a Dimension 3100 microscope (Bruker AXS, U.S.) placed in a N_2 glove box and operated with a Nanoscope IVa controller and equipped with a XYZ Hybrid scan head using Olympus OMCL TS-160/TS-240 cantilever in tapping mode. Analyses have been performed using NanoScope Analysis software (version 1.4, Bruker AXS, U.S.). Transmission electron microscopy (TEM) investigations were conducted on an FEI Tecnai F20 instrument equipped with a Schottky emitter operated at 200 kV. The images were acquired in unfiltered TEM bright field mode using a 2k by 2k UltraScan camera integrated in a Gatan Tridiem post column Imaging Filter. The EBID simulation[44,53−55] combines a single scattering Monte Carlo electron-solid interaction simulation with a precursor handling routine which emulates in this case a Langmuir type adsorption and desorption, random walk surface diffusion, and dissociation based on an extrapolated cross-section as determined by van Dorp et al.[56] The simulation parameters used were: 5 keV beam energy, 25 pA beam current, 1.5 mTorr and sticking coefficient of 1 for the $MeCpPt(IV)Me_3$ precursor. The desorption time was assumed to be 100 ms which is consistent with the estimated $(CH_3)3Pt(CPCH_3)$ binding energy, as well as those determined from other focused beam growth studies.[42,57,58] The equilibrium coverage under these precursor conditions yielded a surface coverage of ~6%. A silicon substrate was assumed and the deposited material was assumed to be PtC_5. For the flat silicon substrate starting material and the PtC_5 deposited material, the 5 keV BSE coefficient is 0.64 and 0.56, respectively; and the secondary electron coefficient is 0.5 and 0.35, respectively. Electron beam dwell times of 0.1, 0.5, 1, 2, and 4 ms were simulated and each dwell time was run with and without a $MeCpPt(IV)Me_3$ surface diffusion coefficient of 1×10^{-8} cm^2 s^{-1}.[52]

CONCLUSION

In conclusion, we have demonstrated what determines the achievable lateral resolution during synthesis of functional nanostructures via focused electron beam induced direct write deposition. It is found that the widths of single lines, synthesized from $MeCpPt(IV)Me_3$ precursor on Si bulk substrates, quickly increase within the first 5 nm deposit height followed by more stable line widths for further increasing heights. Correlation with Monte Carlo trajectory simulations revealed that the relevant saturation widths are in good agreement with the lateral radius of backscatter electrons (BSE) generated in the growing deposit. The related threshold of 2−5 nm line height, for widely constant line widths, corresponds well to the formation of the initial layer the final Pt−C metal-matrix system, consisting of 2−3 nm Pt nano-crystals embedded in a carbon matrix. Correlated simulations concerning the laterally resolved surface coverage during deposition revealed depletion effects at the line center and explain parameter and current dependent variation in the vertical growth rate in agreement with BSE simulations and AFM experiments while lateral resolution is less affected unless low currents are used. Concerning the primary beam energy it is found that 30 keV shows minimal BSE related proximal deposition due to the low BSE yield and the large BSE radius. In contrast, low energy experiments at 5 keV revealed a clear halo formation around the single lines which could clearly be related to the BSE radius of the Si substrate and demonstrates that the use of lower energies reduces the achievable line widths even further. The main finding, however, is that on bulk substrates the chemistry of the deposit itself defines the achievable resolution based on fundamental interaction effects between electrons and the deposited material even for features of less than 5 nm thickness. As the results could be reduced to the interplay of the deposit chemistry and the electron behaviour in solids for a given primary energy, this general concept of resolution limitation is expected to hold for other precursor as well, although different in absolute numbers.

ASSOCIATED CONTENT

Supporting Information

TEM bright field image to visualize the typical Pt grain diameter relevant for the first layer formation; geometrical estimations relevant for AFM tip convolution; CASINO simulations of electron trajectories in the used substrate for 30 and 5 keV at same scales to visualize the different interaction volumes; direct comparison of 4 nm high single lines prepared at 5 keV but at different currents further normalized laterally by the according electron beam diameters to exclude additional, current related broadening effects; lateral expansion of proximal halo deposition together with CASINO simulations to assign the halo to substrate related BSE-S (and SE-II-S) contributions; comparison between experimental and simulated line height evolution for justification of the used coverage simulation. This material is available free of charge via the Internet at http://pubs.acs.org.

AUTHOR INFORMATION

Corresponding Author

*E-mail: harald.plank@felmi-zfe.at. Tel: +43 316 873 8821.

Notes

The authors declare no competing financial interest.

ACKNOWLEDGMENTS

The authors G.A., A.O., G.K. and H.P. gratefully acknowledge the valuable support provided by Prof. Dr. Ferdinand Hofer, DI Roland Schmied, Thomas Ganner, Martina Dienstleder, and Prof. Dr. Werner Grogger. The authors also acknowledge FFG Austria and the Federal Ministry of Economy, Family and Youth of Austria for their financial support (project number 830186). P.D.R. and R.T. acknowledges support from Intel Corporation (and Ted Liang as program mentor) via the direct funding program at the Semiconductor Research Corporation (SRC-2012-In-2310) and matching funds from the Center for Materails Processing. P.D.R. and J.D.F. acknowledge that some of the initial Monte Carlo and precursor simulation algorithms were generated at the Center for Nanophase Materials Sciences, which is sponsored at Oak Ridge National Laboratory by the Scientific User Facilities Division, Office of Basic Energy Sciences, U.S. Department of Energy.

REFERENCES

(1) Utke, I.; Moshkalev, S.; Russell, P. E. *Nanofabrication Using Focused Ion and Electron Beams: Principles and Applications*, 1st ed; Oxford University Press: New York, 2012.

(2) Randolph, S. J.; Fowlkes, J. D.; Rack, P. D. Focused, Nanoscale Electron-Beam-Induced Deposition and Etching. *Crit. Rev. Sol. State* **2006**, *31*, 55−89.

(3) van Dorp, W. F.; Hagen, C. W. A Critical Literature Review Of Focused Electron Beam Induced Deposition. *J. Appl. Phys.* **2008**, *104*, 081301-1−081301-42.
(4) van Dorp, W.; Hansen, T. W.; Wagner, J. B.; De Hosson, J. T. B. The Role Of Electron-Stimulated Desorption In Focused Electron Beam Induced Deposition. *Beilstein J. Nanotechnol.* **2013**, *4*, 474−480.
(5) Botman, A.; Mulders, J. J. L.; Hagen, C. W. Creating Pure Nanostructures From Electron-Beam-Induced Deposition Using Purification Techniques: A Technology Perspective. *Nanotechnology* **2009**, *20*, 372001.
(6) Utke, I.; Gölzhäuser, I. Small, Minimally Invasive, Direct: Electrons Induce Local Reactions Of Dsorbed Functional Molecules On The Nanoscale. *Angew. Chem., Int. Ed.* **2010**, *49*, 9328−9330.
(7) Plank, H.; Gspan, C.; Dienstleder, M.; Kothleitner, G.; Hofer, F. The Influence Of Beam Defocus On Volume Growth Rates For Electron Beam Induced Platinum Deposition. *Nanotechnology* **2008**, *19*, 485302.
(8) Plank, H.; Haber, T.; Gspan, C.; Kothleitner, G.; Hofer, F. Chemical Tuning Of Ptc Nanostructures Fabricated Via Focused Electron Beam Induced Deposition. *Nanotechnology* **2013**, *24*, 1753605.
(9) Heerkens, C. T. H.; Kamerbeek, M. J.; van Dorp, W.; Hagen, C. W.; Hoekstra, J. Electron Beam Induced Deposited Etch Masks. *Microelectron. Eng.* **2009**, *86*, 961−964.
(10) Guan, Y.; Fowlkes, J. D.; Retterer, S. T.; Simpson, M. L.; Rack, P. D. Pulsed Laser Dewetting Of Nickel Catalyst For Carbon Nanofiber Growth. *Nanotechnology* **2008**, *19*, 505302.
(11) Lassiter, M. G.; Liang, T.; Rack, P. D. Inhibiting Spontaneous Etching Of Nanoscale Electron Beam Induced Etching Features: Solutions For Nanoscale Repair Of Extreme Ultraviolet Lithography. *J. Vac. Sci. Technol. B* **2008**, *26*, 963−967.
(12) Liang, T.; Frendberg, E.; Lieberman, B.; Stivers, A. Advanced Photolithographic Mask Repair Using Electron Beams. *J. Vac. Sci. Technol. B* **2005**, *23*, 3101−3105.
(13) Edinger, K.; Becht, H.; Bihr, J.; Boegli, V.; Budach, M.; Hofmann, T.; Koops, H. W. P.; Kuschnerus, P.; Oster, J.; Spies, P.; Weyrauch, B. Electron-Beam-Based Photomask Repair. *J. Vac. Sci. Technol. B* **2004**, *22*, 2902−2906.
(14) Perentes, A.; Bachmann, A.; Leutenegger, M.; Utke, I.; Sandu, C.; Hoffmann, P. Focused Electron Beam Induced Deposition Of A Periodic Transparent Nano-Optic Pattern. *Microelectron. Eng.* **2004**, *73-74*, 412−416.
(15) Utke, I.; Jenke, M. G.; Roling, C.; Thiesen, P.H.; Iakovlev, V.; Sirbu, A.; Mereuta, A.; Caliman, A.; Kapon, E. Polarisation Stabilisation Of Vertical Cavity Surface Emitting Lasers By Minimally Invasive Focused Electron Beam Triggered Chemistry. *Nanoscale* **2011**, *3*, 2718−2722.
(16) Mackus, A. J. M.; Mulders, J. J. L.; van de Sanden, M. C. M.; Kessels, W. M. M. Local Deposition Of High-Purity Pt Nanostructures By Combining Electron Beam Induced Deposition And Atomic Layer Deposition. *J. Appl. Phys.* **2010**, *107*, 116102.
(17) Gavagnin, M.; Wanzenboeck, H. D.; Belić, D.; Bertagnolli, E. Synthesis Of Individually Tuned Nanomagnets For Nanomagnet Logic By Direct Write Focused Electron Beam Induced Deposition. *ACS Nano* **2013**, *7*, 777−784.
(18) Gabureac, M.; Bernau, L.; Boero, G.; Utke, I. Single Superparamagnetic Bead Detection And Direct Tracing Of Bead Position Using Novel Nanocomposite Nano-Hall Sensors. *IEEE Trans. Nanotechnol.* **2013**, *12*, 668−673.
(19) Serrano-Ramon, L.; Cordoba, R.; Rodriguez, L. A.; Magen, C.; Snoeck, E.; Gatel, C.; Serrano, I.; Ibarra, M. R.; De Teresa, J. M. Ultrasmall Functional Ferromagnetic Nanostructures Grown By Focused Electron-Beam-Induced Deposition. *ACS Nano* **2011**, *5*, 7781−7787.
(20) Fernandez-Pacheco, A.; De Teresa, J. M.; Cordoba, R.; Ibarra, M. R.; Petit, D.; Read, D. E.; O'Brien, L.; Lewis, E. R.; Zeng, H. T.; Cowburn, R. P. Domain Wall Conduit Behavior In Cobalt Nanowires Grown By Focused Electron Beam Induced Deposition. *Appl. Phys. Lett.* **2009**, *94*, 192509-1−192509-3.
(21) Gabureac, M.; Bernau, L.; Utke, I.; Boero, G. Granular Co−C Nano-Hall Sensors By Focused-Beam-Induced Deposition. *Nanotechnology* **2010**, *21*, 115503.
(22) Porrati, F.; Sachser, R.; Schwalb, C. H.; Frangakis, A. S.; Huth, M. Tuning The Electrical Conductivity Of Pt-Containing Granular Metals By Postgrowth Electron Irradiation. *J. Appl. Phys.* **2011**, *109*, 0637151-1−063715-7.
(23) Huth, M.; Porrati, F.; Schwalb, C.; Winhold, M.; Sachser, R.; Dukic, M.; Adams, J.; Fantner, G. Focused Electron Beam Induced Deposition: A Perspective. *Beilstein. J. Nanotechnol.* **2012**, *3*, 597.
(24) Kolb, F.; Schmoltner, K.; Huth, M.; Hohenau, A.; Krenn, J.; Klug, A.; List, E. J. W.; Plank, H. Variable Tunneling Barriers In FEBID Based Ptc Metal-Matrix Nanocomposites As A Transducing Element For Humidity Sensing. *Nanotechnology* **2013**, *24*, 305501.
(25) van Dorp, W.; Zhang, X.; Feringa, B. L.; Hansen, T. W.; Wagner, J. B.; De Hosson, J. T. B. Molecule-By-Molecule Writing Using A Focused Electron Beam. *ACS Nano* **2012**, *6*, 10076−10081.
(26) van Dorp, W. F.; van Someren, B.; Hagen, C. W.; Kruit, P.; Crozier, P. A. Approaching The Resolution Limit Of Nanometer-Scale Electron Beam-Induced Deposition. *Nano Lett.* **2005**, *5*, 1303−1307.
(27) Tanaka, M.; Shimojo, M.; Han, M.; Mistuishi, K.; Furuya, K. Ultimate Sized Nano-Dots Formed By Electron Beam-Induced Deposition Using An Ultrahigh Vacuum Transmission Electron Microscope. *Surf. Interface Anal.* **2005**, *37*, 261−264.
(28) Bret, T.; Utke, I.; Hoffmann, P.; Abourida, M.; Doppelt, P. Electron Range Effects In Focused Electron Beam Induced Deposition Of 3D Nanostructures. *Microelectron. Eng.* **2006**, *83*, 1482−1486.
(29) Van Dorp, W. F.; Hagen, C. W.; Crozier, P. A.; Kruit, P. Growth Behavior Near The Ultimate Resolution Of Nanometer-Scale Focused Electron Beam-Induced Deposition. *Nanotechnology* **2008**, *19*, 225305.
(30) Córdoba, R.; Baturina, T. I.; Sesé, J.; Yu Mironov, A.; De Teresa, J. M.; Ibarra, M. R.; Nasimov, D. A.; Gutakovskii, A. K.; Latyshev, A. V.; Guillamón, I.; Suderow, H.; Vieira, S.; Baklanov, M. R.; Palacios, J. J.; Vinokur, V. M. Magnetic Field-Induced Dissipation-Free State In Superconducting Nanostructures. *Nat. Commun.* **2013**, *4*, 1437−1439.
(31) van Dorp, W. F.; Beyer, A.; Mainka, M.; Gölzhäuser, G.; Hansen, T.W.; Wagner, J.B.; Hagen, C.W.; De Hosson, J. T. M. Focused Electron Beam Induced Processing And The Effect Of Substrate Thickness Revisited. *Nanotechnology* **2013**, *24*, 345301.
(32) van Dorp, W. F.; van Someren, B.; Hagen, C. W.; Kruit, P.; Crozier, P. A. Approaching The Resolution Limit Of Nanometer-Scale Electron Beam-Induced Deposition. *Nano Lett.* **2005**, *5*, 1303−1307.
(33) Crozier, P. A.; Tolle, J.; Kouvetakis, J.; Ritter, C. Synthesis Of Uniform Gan Quantum Dot Arrays Via Electron Nanolithography Of D_2gan_3. *Appl. Phys. Lett.* **2004**, *84*, 3441−3443.
(34) Fujita, J.; Ishida, M.; Ichihashi, T.; Ochiai, Y.; Kaito, T.; Matsui, S. Carbon Nanopillar Laterally Grown With Electron Beam-Induced Chemical Vapor Deposition. *J. Vac. Sci. Technol. B* **2003**, *21*, 2990−2993.
(35) Van Oven, J. C.; Berwald, F.; Berggren, K. K.; Kruit, P.; Hagen, C. W. Electron-Beam-Induced Deposition Of 3-nm-Half-Pitch Patterns On Bulk Si. *J. Vac. Sci. Technol. B* **2011**, *29*, 06F305-1−06F305-6.
(36) Utke, I.; Gölzhäuser, I. Small, Minimally Invasive, Direct: Electrons Induce Local Reactions Of Adsorbed Functional Molecules On The Nanoscale. *Angew. Chem. Int. Ed.* **2010**, *49*, 9328−9330.
(37) Utke, I.; Friedli, V.; Purrucker, M.; Michler, J. Resolution In Focused Electron- And Ion-Beam Induced Processing. *J. Vac. Sci. Technol. B* **2007**, *25*, 2219−2223.
(38) Fowlkes, J. D.; Rack, P. D. Fundamental Electron−Precursor−Solid Interactions Derived From Time-Dependent Electron-Beam-Induced Deposition Simulations And Experiments. *ACS Nano* **2010**, *4*, 1619−1629.
(39) Smith, D. A.; Fowlkes, J. D.; Rack, P. D. Understanding The Kinetics And Nanoscale Morphology Of Electron-Beam-Induced Deposition Via A Three-Dimensional Monte Carlo Simulation: The Effects Of The Precursor Molecule And The Deposited Material. *Small* **2008**, *4*, 1382−1389.

(40) Fowlkes, J. D.; Randolph, S. J.; Rack, P. D. Growth And Simulation Of High-Aspect Ratio Nanopillars By Primary And Secondary Electron-Induced Deposition. *J. Vac. Sci. Technol. B* **2005**, *23*, 2825−2832.
(41) van Dorp, W. F.; Wnuk, J. D.; Gorham, J. M.; Fairbrother, D. H.; Madey, T. E.; Hagen, C. W. Electron Induced Dissociation Of Trimethyl (Methylcyclopentadienyl) Platinum (IV): Total Cross Section As A Function Of Incident Electron Energy. *J. Appl. Phys.* **2009**, *106*, 74903-1−74903-9.
(42) Wnuk, J. D.; Gorham, J. M.; Rosenberg, S. G.; van Dorp, W. F.; Madey, T. E.; Hagen, C. W.; Fairbrother, D. H. Electron Induced Surface Reactions Of The Organometallic Precursor Trimethyl-(Methylcyclopentadienyl)-Platinum(IV). *J. Phys. Chem. C* **2009**, *113*, 2487−2496.
(43) Plank, H.; Smith, D. A.; Haber, T.; Rack, P. D.; Hofer, F. Fundamental Proximity Effects In Focused Electron Beam Induced Deposition. *ACS Nano* **2012**, *6*, 286−294.
(44) Smith, D. A.; Fowlkes, J. D.; Rack, P. D. Simulating The Effects Of Surface Diffusion On Electron Beam Induced Deposition Via A Three-Dimensional Monte Carlo Simulation. *Nanotechnology* **2008**, *19*, 415704.
(45) Goldstein, J.; Newbury, D.; Joy, D.; Lyman, C.; Echlin, P.; Lifshin, E.; Sawyer, L. Michael, J. *Scanning Electron Microscopy and X-Ray Microanalysis*, 2nd ed; Springer Science + Business Media Inc.: New York, 2003.
(46) Plank, H.; Michelitsch, S. G.; Gspan, C.; Hohenau, A.; Krenn, J.; Kothleitner, G.; Hofer, F. Optimization Of Postgrowth Electron-Beam Curing For Focused Electron-Beam-Induced Pt Deposits. *J. Vac. Sci. Technol. B* **2011**, *29*, 051801-1−051801-7.
(47) Bret, T.; Utke, I.; Gaillard, C.; Hoffmann, P. Periodic Structure Formation By Focused Electron-Beam-Induced Deposition. *J. Vac. Sci. Technol. B* **2004**, *22*, 2504−2510.
(48) Bret, T.; Utke, I.; Hoffmann, P. Influence Of The Beam Scan Direction During Focused Electron Beam Induced Deposition Of 3D Nanostructures. *Microelectron. Eng.* **2005**, *78*, 307−313.
(49) Bret, T.; Utke, I.; Hoffmann, P.; Abourida, M.; Doppelt, P. Electron Range Effects In Focused Electron Beam Induced Deposition Of 3D Nanostructures. *Microelectron. Eng.* **2006**, *83*, 1482−1486.
(50) Drouin, D.; Couture, A. R.; Joly, D.; Tastet, C.; Aimez, V.; Gauvin, R. A Fast And Easy-To-Use Modeling Tool For Scanning Electron Microscopy and Microanalysis Users. *Scanning* **2007**, *29*, 92−101.
(51) Derived from contrast transfer functions, FEI, The Netherlands
(52) Winkler, R.; Fowlkes, J.D.; Szkudlarek, A.; Utke, I.; Rack, P.D.; Plank, H. The Nanoscale Implications Of A Molecular Gas Beam During Electron Beam Induced Deposition. *ACS Appl. Mater. Interfaces* **2014**, *6*, 2987−2995.
(53) Fowlkes, J. D.; Rack, P. D. . Fundamental Electron-Precursor-Solid Interactions Derived From Time-Dependent Electron-Beam-Induced Deposition Simulations And Experiments. *ACS Nano* **2010**, *4*, 1619−1629.
(54) Smith, D.A.; Joy, D.; Rack, P.D. Monte Carlo Simulation Of Focused Helium Ion Beam Induced Deposition. *Nanotechnology* **2010**, *21*, 175302.
(55) Smith, D.A.; Fowlkes, J. D.; Rack, P.D. A Nanoscale Three-Dimensional Monte Carlo Simulation Of Electron-Beam-Induced Deposition With Gas Dynamics. *Nanotechnology* **2007**, *18*, 265308.
(56) van Dorp, W.F. The Role Of Electron Scattering In Electron-Induced Surface Chemistry. *Phys. Chem. Chem. Phys.* **2012**, *14*, 16753−16759.
(57) Utke, I.; Hoffmann, P.; Melngailis, J. Gas-Assisted Focused Electron Beam And Ion Beam Processing And Fabrication. *J. Vac. Sci. Technol. B* **2008**, *26*, 11971276.
(58) Alkemade, P. F. A.; Miro, H.; van Veldhoven, E.; Maas, D.J.; Smith, D.A.; Rack, P.D. Quantitative Simulation Of Ion-Beam Induced Deposition Of Nanostructures. *J. Vac. Sci. Technol. B* **2011**, *29*, 06FG05-1−06FG05-7.